

**Mixing in the extratropical stratosphere:
Model-measurements comparisons using MLM diagnostics**

Jun Ma, Darryn W. Waugh

Johns Hopkins University, Baltimore, Maryland

Anne R. Douglass, Stephan R. Kawa

NASA Goddard Space Flight Center, Greenbelt, Maryland

Short title: MIXING AND TRANSPORT IN STRATOSPHERE: A COMPARISON

**Mixing in the extratropical stratosphere:
Model-measurements comparisons using MLM diagnostics**

Jun Ma, Darryn W. Waugh, Anne R. Douglass, Stephan R. Kawa

Summary

In this study, we have performed a model-measurement comparison based on the seasonal distribution of the equivalent length (ξ). This diagnostic provides a way to quantify mixing in the stratosphere from the distribution of long-lived tracers.

We choose N_2O measurements from UARS CLAES as our comparison benchmark and compare it with N_2O CTM simulations advected by GCM winds (MACCM2 and GSFC SKYHI) and assimilated winds (GEOS DAS). Important dynamical features, such as polar vortices and surf zone, are identified in both the measurements and model simulations. Differences among the models are shown with regard to the details in structure and evolution of isentropic tracer transport barriers, as identified by the low value of equivalent length. High equivalent length in the summer hemispheres is unanimously observed in both the measurements and the models.

Artificial tracer experiments are conducted with the GEOS DAS winds. Comparison between this artificial tracer run and N_2O run reveals some difference in their equivalent length distribution. The implication of these differences are discussed.

Abstract.

We evaluate transport processes in the extratropical lower stratosphere for both models and measurements with the help of equivalent length diagnostic from the modified Lagrangian-mean (MLM) analysis. This diagnostic is used to compare measurements of long-lived tracers made by the Cryogenic Limb Array Etalon Spectrometer (CLAES) on the Upper Atmosphere Research Satellite (UARS) with simulated tracers. Simulations are produced in Chemical and Transport Models (CTMs), in which meteorological fields are taken from the Goddard Earth Observing System Data Assimilation System (GEOS DAS), the Middle Atmosphere Community Climate Model (MACCM2), and the Geophysical Fluid Dynamics Laboratory (GFDL) "SKYHI" model, respectively. Time series of isentropic equivalent length show that these models are able to capture major mixing and transport properties observed by CLAES, such as the formation and destruction of polar barriers, the presence of surf zones in both hemispheres. Differences between each model simulation and the observation are examined in light of model performance. Among these differences, only the simulation driven by GEOS DAS shows one case of the "top-down" destruction of the Antarctic polar vortex, as observed in the CLAES data. Additional experiments of isentropic advection of artificial tracer by GEOS DAS winds suggest that diabatic movement might have considerable contribution to the equivalent length field in the 3D CTM diagnostics.

1. Introduction

The mixing and transport properties of the stratosphere, particularly those of the lower to middle stratosphere, have been the focus of intensive scientific attention recently. Over the past two decades, a large database of global measurements of atmospheric constituents in the stratosphere has been accumulated, and General Circulation Models (GCMs) and Chemical Transport Models (CTMs) have been developed with emphasis on the stratosphere. Furthermore, data assimilation provides meteorological fields that represent the stratosphere realistically and satisfy the equations of motion by combining measurements with a GCM.

The expansion of the stratospheric database and the large quantities of output from model simulations stimulate the need for more quantitative diagnostic tools. The recently developed modified Lagrangian-mean (MLM) [*Nakamura, 1995, 1998; Haynes and Shuckburgh, 2000a*] technique provides such a tool. This diagnostic generalizes the idea of the area coordinate proposed by *Butchart and Remsberg [1986]*, and can be applied to all stratospheric tracers with a monotonic pole-to-equator trend in its zonal-mean distribution. The essential idea of MLM diagnostic is the substitution of geographic latitude with the equivalent latitude, which quantifies the area enclosed by tracer contours. The equivalent latitude thus defined resembles the usual latitude except when strong zonal asymmetry develops. When mapping a long-lived stratospheric tracer onto a two-dimensional meridional cross section, the equivalent latitude excels over geographic latitude by providing a meridional coordinate that is transparent to the

reversible tracer variation over isentropic surfaces.

Another advantage of the MLM diagnostic is its precise representation of effective diffusivity with the isentropic equivalent length [Nakamura, 1995]. Unlike the traditional counterpart K_{yy} in the transformed Eulerian-mean (TEM) model, this equivalent length provides an objective measure of the scrambledness of a tracer contour. It can be calculated directly from a snapshot of the global tracer distribution without knowledge of the wind field [Nakamura, 1998]. Recently Haynes and Shuckburgh [2000a, 2000b] and Allen and Nakamura [2001] have extended the application of equivalent length (or *effective diffusivity*) to an artificial tracer advected by assimilated winds, and derive mixing and transport properties of the atmosphere from the equivalent length of such artificial tracer.

The vast database of global tracer distribution accumulated from satellite measurements and the tracer simulations produced from various models provide an opportunity to test and apply the MLM diagnostic. In the past, MLM diagnostic have been applied to N₂O from Geophysical Fluid Dynamics Laboratory (GFDL) SKYHI GCM [Nakamura, 1995], and Upper Atmosphere Research Satellite (UARS) Cryogenic Limb Array Etalon Spectrometer (CLAES) [Nakamura and Ma, 1997] (hereafter NM97), an artificial tracer advected by European Centre for Medium-Range Weather Forecasting (ECMWF) wind [Haynes and Shuckburgh, 2000a, 2000b], and an artificial tracer advected by winds from United Kingdom Meteorological Office (UKMO) [Allen and Nakamura, submitted]. In this paper, we focus on the use of the MLM diagnostic as an assessment of 3D CTMs. We choose long-lived tracers from the following models for

this study: a CTM driven by winds from the Goddard Earth Observing System Data Assimilation System (GEOS DAS) [Douglass *et al.*, 1997]; a CTM driven by the output from the Middle Atmosphere Community Climate Model (MACCM2) [Boville, 1995]; and the Geophysical Fluid Dynamics Laboratory (GFDL SKYHI) GCM [Hamilton *et al.*, 1995].

Different data sets have different advantages and disadvantages. Satellite measurements, such as UARS CLAES, provide realistic data distribution but with relatively low resolution and limited spacial and temporal coverage. Tracers simulated within a GCM (or from a CTM driven by the output from a GCM) have high spatial resolution and consistent dynamical fields, but the dynamical fields may exhibit biases relative to observations. Interannual variability is ignored when only a single year's GCM output is utilized. Tracers from a CTM driven by assimilated winds have high resolution and realistic seasonal and interannual variations. Combining the observations with a general circulation model produces realistic temperature and horizontal winds, but derived fields such as the residual circulation may not be internally consistent with the heating rates. In this paper, we will analyze chemical tracer distributions from all the three categories and compare them among each other, especially between model and measurements. We focus on the seasonal variation of mixing and transport efficiency in the extratropical lower stratosphere diagnosed from the equivalent length of inert tracers, and the formation and destruction of the polar vortices. A subset experiment of advecting artificial passive tracer on isentropic surfaces is also conducted. These diagnostics are utilized to provide a quantitative evaluation of model performances.

Section 2 describes briefly the basic idea of MLM, including the definition of equivalent length. In section 3, MLM analysis of UARS CLAES measurements are revisited with the help of time series of equivalent length. We also compare the equivalent length calculation from CLAES measurement of N_2O and CH_4 . Though this satellite data set has limited spatial resolution and incomplete spatial and temporal coverage, the CLAES provides the most complete global tracer measurements available so far and we will use it as a standard for our model inter-comparisons. The equivalent length of N_2O from the CTM driven by GEOS DAS winds are analyzed and compared with that from CLAES N_2O in section 4. MACCM2 and SKYHI results are presented in section 5. Section 6 continues to analyze GSFC assimilation with an artificial tracer advection, cross inspection of this two dimensional result with three dimensional result of section 3 provides more insight to the model performance. A summary of this work is presented in the last section.

2. Equivalent length diagnostics

In the MLM view of long-lived tracer distributions, the three dimensional tracer field is decomposed onto isentropic layers. On each isentrope, the area enclosed by tracer contours replaces the geographic latitude as the new meridional coordinate. Tracer contours enclosing the *same* area can have *different* shapes, and therefore *different* contour length. *Given the area*, the length of a tracer contour cannot be shorter than the perimeter of a perfect circle on the isentrope, but there is no upper limit to the possible length that a tracer contour can have. This is described by the fractal dimension of the

contour line. The equivalent length L_e is thus defined to reflect this behavior:

$$L_e^2(A, t) \equiv |\hat{\nabla}q|^2 \left(\frac{\partial q}{\partial A} \right)^{-2} \quad (1)$$

where q is the concentration of a tracer, A is the area occupied by all tracer with concentration less (or greater, depending on the tracer's pole-to-equator trend) than or equal to q , and $(\hat{\cdot})$ is defined as the average of any scalar around the tracer contour. The areal gradient $\partial q/\partial A$ measures mixedness of the tracer, and vanishes in a perfectly homogeneous state.

The relationship between L_e and the horizontal diffusivity can be appreciated by the following two dimensional advection diffusion equation in the area coordinate on an isentrope [Nakamura, 1998]:

$$\frac{\partial}{\partial t}q(A, t) = \frac{\partial}{\partial A} \left(DL_e^2 \frac{\partial q}{\partial A} \right) \quad (2)$$

where D is the constant microscale diffusion coefficient. It is clear that the stretching or shrinking of L_e^2 measures the efficiency of cross-mass transport of tracer.

In equation (2), the diffusion is proportional to L_e^2 , which in effect is the square of the normalized tracer contour length (see Nakamura, [1998] for a detailed discussion). The area coordinate can be transformed to an equivalent latitude $\phi_e = \sin^{-1}(1 - A/2\pi a^2)$ (a is Earth's radius) to facilitate the comparison with geographical latitude, and the L_e can be replaced with a non-dimensional number,

$$\xi = L_e^2/L_0^2, \quad (3)$$

where $L_0(\phi_e) = 2\pi a \cos \phi_e$, is the length of a perfect circle on the isentrope that encloses the same amount of area as L_e does. In the following discussion, we will extensively employ ϕ_e and ξ to diagnose mixing and transport properties of the stratosphere.

3. UARS CLAES measurements

In this paper we use the version 9 data of the CLAES trace constituents. Version 7 data was used in the previous MLM analysis of CLAES N_2O by NM97, and the differences between the two versions are minor. For a description of the CLAES experiment, see *Roche et al.* [1993]. In this section we summarize the overall characteristics of MLM analysis, with an emphasis on the time series of ξ on different isentropes. Some of the observations made in NM97 are reiterated here.

3.1. CLAES N_2O diagnostic

Stratospheric long-lived tracers, such as N_2O and CH_4 , have monotonic zonal mean isentropic distribution from equator to both poles, therefore they can be mapped into the ϕ_e space in each hemisphere. However the local extremum in the tropics creates a difficulty in constructing a global ϕ_e coordinate for such long-lived tracers. Inspired by the down-gradient diffusive flux of tracers, *Ma* [1999] used an expedient way to patch together ϕ_e from two separate hemispheres into a continuous one by assuming the equivalent equator as the water dividing line on the three dimensional topography

formed by tracer isosurfaces. Under many situations, this has proven to be a better way to find the equivalent equator, though it should not be taken as a unique definition of hemispheric boundary. In this work, we use this method to construct global MLM maps for both N_2O and CH_4 .

In NM97 stratosphere mixing was investigated by examining potential temperature-equivalent latitude ($\theta - \phi_e$) cross section of ξ for given dates (see Plates 2 and 3 of NM97; see also Plate 3 below). Here we focus on the temporal evolution of ξ on isentropic surfaces. We choose three isentropic surfaces of 600K, 800K, and 1000K for our model measurement comparison, and 800K is emphasized for the sake of space limit. The following observations are made out of careful examination of these two kinds of plots. Unless otherwise stated, ξ is calculated from N_2O .

Plate 1 shows the evolution of ξ on the 600, 800, and 1000K surfaces. Also shown is the zonal-mean zonal wind from the National Center for Environmental Prediction (NCEP) reanalyses [*Kalnay et al.*, 1996] to help understand the relationship between the mixing and the wind structure (note that the vertical coordinate in Plate 1 is ϕ_e for ξ and geographic latitude for winds).

In both summer hemispheres there is a single stepwise structure, with a subtropical area of low ξ and high ξ throughout the rest of mid to high latitudes (see also Plate 2a, 3a, 4d, and 5d of NM97). During the fall, the subtropical region of low ξ is still present but shrinks a little bit towards equivalent equator, and the same time another patch of low ξ starts to develop in the high latitudes. The low ξ in the high latitudes becomes well-developed in the winter and corresponds to the edge of winter polar

vortices (compare with strong zonal winds). Meanwhile, the subtropical area of low ξ reduces to its minimal value and a well-contained area of high ξ sandwiched by the two ξ minima corresponds to the surf zone [McIntyre and Palmer 1984]. In spring, both the subtropical region of low ξ and high latitude region of low ξ begin to move polarwards, until the high latitude low ξ completely disappears along with the polar night jet and the hemispheric distribution of ξ returns to the summer single stepwise structure. Taking the low value of ξ as indication of isentropic transport barrier [Nakamura 1996], the above-mentioned seasonal variation of ξ shows a wide perennial barrier zone in the tropics with seasonal varying meridional width (which is consistent with Plumb's [1996] "tropical pipe" model) and a winter polar barrier alternating at each hemisphere.

Plate 1 also shows large effective diffusivity in the summer extratropics, especially in the lower stratosphere. While the ξ in the northern summer is modestly high ($\xi \sim 1.5$ on 600K), the southern hemispheric ξ has a distinct maximum during summer season ($\xi \sim 2.2+$ on 600K), comparing with $\xi \sim 1.6$ (southern winter surf zone) and 2.4 (northern winter surf zone). If the large amplitude of ξ in January/February 1992 is suspicious of contamination caused by the Pinatubo eruption (see discussion below), the southern hemispheric ξ in January/February 1993 still shows a noticeable maximum, even larger than the value of ξ of the surf zone in July/August 1992. The high effective diffusivity in the summer extratropical stratosphere is also diagnosed by others in the lower to middle stratosphere, for example, Allen and Nakamura [2001] Haynes and Shuckburgh [2000a, 2000b].

Plate 1 also reveals several interesting features regarding the Arctic and Antarctic

polar vortices. First the vertical variation of the formation/decay differs between hemispheres. During both the formation and decay stage of the Antarctic polar vortex, the edge of the polar vortex (as indicated by the dark blue track in the high latitudes) appears and disappears from the top down. This is in accordance with the earlier appearance of the polar night jet in the upper stratosphere (see the overlaid zonal mean zonal wind in Plate 1). The thick purple lines in Plate 2 show ξ from UARS N_2O on 6 isentropic surfaces for June 17 and November 8 1992. ξ on June 17 1992 (left panel) illustrates the earlier formation of Antarctic polar vortex (the vortex edge denoted by low ξ already approaches $\phi_e = -50^\circ$ on 1000 K, while on lower levels its presence lags towards the pole, and on 500 K, it is still not yet formed), while ξ on November 8 1992 (right panel) shows a similar gradual decay of Antarctic polar vortex with the altitude. In November, the vortex edge is around $\phi_e = -70^\circ$ at 500K, and retreats towards the pole with increasing altitude). *Waugh and Randel* [1999] illustrated the same top-down structure of Antarctic polar vortex using elliptical diagnostics. This top-down formation and decay of polar vortex is not at all clear for the northern hemisphere. This might have something to do with the dynamically active nature of northern polar vortex.

A second feature is the area of the polar vortices. Plate 1 shows that the Antarctic polar vortex extends further equatorward than the Arctic polar vortex during their mature stage. For example, at 1000 K, the Antarctic polar vortex extends beyond $\phi_e = -50^\circ$ in August, while the Arctic polar vortex is well within polarward of $\phi_e = 55^\circ$ throughout its lifetime.

Plate 1 also implies different origins for polar barriers in the upper and lower

stratosphere, especially in the southern hemisphere. For example, at 600 K, the Antarctic polar barrier first appears in the polar region, then it moves equatorward to $\phi_e = -45^\circ$ in late June, and then moves back towards the pole during September, and finally disappears by the end of November. On this isentropic surface, the polar barrier is surrounded by a mixing zone during its entire lifetime. At higher isentropic surfaces, not only does the Antarctic polar barrier form and end earlier (as discussed above), but the mid-latitude mixing zone seems to be interrupted from April to June by a second transport barrier originating in the subtropics. Such interruption is clear on the 1000K surface, even with the missing May observation. It is not as clear on the 800K surface. The 600K shows a continuous Antarctic polar barrier from April to June, and the continuation is clearly interrupted on the 1000K, the ambiguous 800K observation seems to fit in the picture that there is a transition from the sole origin of polar barrier at the lower stratosphere to a dual origins at higher stratosphere.

3.2. CLAES CH₄ – N₂O comparison

CLAES also measured methane (CH₄), which like N₂O is a long-lived tracer with tropospheric source and stratospheric sink. We now examine the sensitivity of the ξ calculation to the long-lived tracer used.

Plate 3 shows ξ calculated from N₂O and CH₄ for two periods exactly a year apart (January 25-27, 1992 and 1993). While there is good agreement for 1993 between ξ from CH₄ and N₂O, there are notable differences at altitude and low latitudes in 1992.

This can be clearly seen in Figure 1, which shows the mean difference between

ξ calculated from N_2O and CH_4 . Generally the mean deviation is under 1 with the exception being the early period where large differences are found (particularly at 600K). The large difference at 600K decreases steadily with time in the initial one year period. It is not clear whether this is due to instrument performance or the presence of the sulfate layer due to Mount Pinatubo eruption. The reduced amplitude of the mean deviation with time and altitude seems to favor the volcano contamination assumption. *Roche et al.* [1996] pointed out the possible influence of a sulfate layer to the CLAES measurements in his validation of CLAES N_2O and CH_4 . He concluded that CLAES CH_4 has a larger random error than CLAES N_2O in the lower stratosphere.

The small overall difference between ξ obtained from two different CLAES long-lived tracer measurements, after the first 100 days, adds to our confidence of utilizing the CLAES N_2O 's ξ as the standard for the following model measurement comparison. Note, we also compared the simulated N_2O and CH_4 from the models cited below, and the general difference between the two is even smaller than what is observed by CLAES. For example, the mean deviation between ξ calculated from N_2O and CH_4 of GSFC 1998/99 run (not shown) is generally less than 0.2, 0.2, and 0.1 on 600K, 800K, and 1000K respectively.

3.3. Seasonal variability

UARS CLAES measurements lasted from October 1991 to May 1993. This period includes two southern hemisphere summers and two northern hemisphere winters, and so CLAES measurements can be used in some degree to analyze interannual variability

of mixing and transport properties in the stratosphere. Plate 1 suggests larger seasonal variability of ξ on the lower isentropic surfaces and in the southern hemisphere.

However, we need to keep in mind of the Mount Pinatubo eruption in late 1991 and the large $\text{CH}_4 - \text{N}_2\text{O}$ difference in the initial part of the record on 600K (Figure 1).

We first consider variability at each individual isentropic surfaces. The largest interannual variability is found on the 600K isentropic surface. The ξ maximum for the southern hemisphere from November to March has a larger peak value and broader area in 1992 than 1993. This interannual variability is also found on the 800K isentropic surface but with a less amplitude. Besides this, the northern hemisphere surf zone (December) shows a larger ξ in 92/93 than 91/92 on the 800K isentropic surface. On the 1000K isentropic surface, the amplitude of interannual variability is small for both northern and southern hemispheres.

The ξ distribution from late 1992 to early 1993 for the northern hemisphere has nearly identical structure as that of the previous year, even with the similar minor warming effects. The small interruption of ξ minimum around the Arctic polar region at January 1992 (800K and 1000K) and March 1993 are identified as minor stratospheric warmings [*Manney et al.* 1993, *Kumer et al.*, 1995]. The only noticeable interannual variability for northern hemisphere is perhaps on the 800K surface around March. ξ appears to have a larger maximum around $\phi_e = 50^\circ$ during March 1993 than occurs during March 1992. Considering the dynamically active northern hemisphere, the lack of strong variability between winters may be surprising. However, this lack of interannual variability, is consistent with the previous analysis by *Zurek et al.* [1996]. *Zurek et al.*

showed that the minimum vortex temperature and the isolation of Arctic polar vortex at 450K revealed similarity between the 91/92 and 92/93 winters.

There is also some interannual variability in the vertical structure of the ξ . In January and February 1992, ξ decreases with height in both the southern hemisphere (summer) and the northern hemisphere surf zone. Whereas in January and February 1993, ξ increases with height in the southern hemisphere and ξ in the northern hemisphere surf zone decreases less rapidly with height. This difference in the vertical structure in the southern hemisphere can be seen in Plate 3.

The changes in vertical structure are due mainly to changes in the lower stratosphere, and this raises again the issue of possible contamination of the data by Mount Pinatubo volcano. In particular, the vertical decrease of the strong ξ in January and February 1992 coincides with the fading effect of volcano effect, and we wonder whether the vertical decreasing trend of ξ is entirely a consequence of volcano eruption. However, *Allen and Nakamura*, [2001] compiled a 7-year (1992-1998) seasonal climatology of effective horizontal diffusivity for the stratosphere. Their result suggests a very large ξ at lower stratosphere for the January, and it decreases sharply with altitude. This seems to suggest our January and February 1992 calculation is more in line with the climatology than our January and February 1993 calculation. At this moment, we still leave the question open as to how much the volcano affects the CLAES N₂O measurement, and thus the ξ calculation based on this measurement. With this uncertainty in mind, we choose 800K isentropic surface as our base surface for model-data comparison base to alleviate any volcanic effect.

4. GSFC 3D chemical transport model

4.1. Model description

We consider now N_2O simulated by the GSFC 3D CTM [Douglass and Kawa, 1999]. This off-line CTM is driven by winds and temperatures from the Goddard Earth Observing System Data Assimilation System (GEOS DAS). Winds and temperature are updated every 6 hours using instantaneous output from the assimilation system. The horizontal resolution of the assimilation winds and temperatures is 2° latitude by 2.5° longitude. The assimilated wind fields are interpolated to the 25 vertical levels between the surface and 1 hPa. The spacing is about 1.5 km up to 20 km and increases to about 4 km above 30 km. There is no explicit sub-grid scale parameterization for mixing in the stratosphere or troposphere. The 1997/98 simulation is driven by “STRAT” winds from the GEOS 1 assimilation from 18 March 1997 to 31 March 1998. The 1998/99 simulation is run with “TRMM” winds from the GEOS 2 for the period 7 October 1998 to 19 December 1999 [Douglass and Kawa, 1999]. The tracer data from CTM output are sampled once every day.

4.2. Equivalent length diagnostic

Plate 4 shows maps of ξ on 800K isentropic surface for N_2O from GSFC 3D CTM runs of (a) 1997/98 and (b) 1998/99. The two experiments are aligned with the same season to facilitate the comparison. The corresponding zonal-mean zonal winds from GEOS DAS are overlaid on the plots.

Comparison of Plate 4 with Plate 1 reveals that many features in the CLAES ξ that are captured by both model runs. These include the development of polar barrier in the autumn and its decay in late winter and early spring (dark blue colors in Plate 4), large ξ in the mid-latitude surf zone as well as inside the Antarctic polar vortex, and the gradual expansion of surf zone ξ maximum to cover the entire (summer) extratropics. The polar barriers first appear in the mid-latitudes during autumn, grow in strength, and then in spring the barriers decay and move towards the poles.

There are also areas of consistent disagreement between CLAES N_2O and the two GSFC CTM runs. First, the rates at which the Antarctic polar barrier expands and shrinks are too small for both GSFC simulations. In the simulations the barrier stays at more or less the same ϕ_e from late April to early November whereas the CLAES observations show that the area enclosed by the Antarctic barrier grows from April to a maximum in August (when it is nearly doubled its size in April), and then shrink back to the original size in November and finally disappears.

Another difference between both GSFC runs and CLAES N_2O observations is the strength of the Arctic polar barriers. In both GSFC runs these barriers are not as clear and systematic as in ξ map from CLAES N_2O . This is related to the sudden warming events that occurred in the winters of 1997/98 and 1998/99. These warming events and other interannual variability will be discussed in the following subsection.

4.3. Interannual variability

The two runs of GSFC CTM cover more than two years and some interannual variation can be observed. Unfortunately, the two GSFC runs were advected by the different assimilation wind systems (the wind field for 1997/98 run is on 37 vertical hybrid pressure levels with six sigma levels at the bottom, while the wind field for 1998/99 run is on 70 terrain-following sigma levels), and some of year-to-year variations may be due to changes in the assimilation system. However, this system-generated variability is likely to be small, and with the help of other observations, we will try to determine the real interannual variability from the two simulations.

The 1998/99 simulation captures the different timing in the destruction of Antarctic polar vortex along the vertical direction. A more detailed comparison between CLAES and among other models is shown in Plate 2. The thin green curve represents the 1998/99 run of GSFC 3D CTM, the thin blue curve represents the 1997/98 run, and the thick purple one the CLAES. During November 1998, the Antarctic vortex edge is located around $\phi_e = -60^\circ$ on 500K isentrope, while the higher it goes, the closer it is towards the pole, for example, on 1000K, it is at about $\phi_e = -75^\circ$. This is the only case in our selected models that the top-down destruction of polar vortex is simulated. None of the models exhibit the same phase lag in the vortex forming stage. Please note that GSFC 1998/99 run sampled two different Antarctic vortex cycles. The formation of another Antarctic polar vortex in the 1998/99 run and both formation and destruction of Antarctic polar vortex in the 1997/98 run do not show such a structure,

as demonstrated clearly in Plate 2.

The most drastic event during 1997-1999 is perhaps the major sudden warming event in December 1998. It was the first major warming in nearly 8 years, and the second major warming observed before the end of December [*Manney et al.* 1999]. It can be identified as a sudden increase of ξ poleward of $\phi_e = 60^\circ$ in Plate 4. The high values of ξ start in mid-December, closely follows the reverse of the polar night jet, and last for less than a month and penetrates all three isentropic surfaces we sampled (600K and 1000K not shown). Low values of ξ at high latitudes resume in January, when the polar night jet recovers from the warming. There is another warming later in February 1999, as evident from the overlaid zonal wind field. This second warming only causes a modest increase of ξ on 600K (not shown) and 800K.

The 1997/98 winter is rather disturbed and has a weak polar night jet, as evident from the overlaid zonal mean wind. This is reflected in the frequently interrupted ξ minimum (Plate 4a). In fact, there is not a clear ξ minimum track for the 1997/98 Arctic polar vortex.

There is an obvious difference of ξ behavior during the two northern hemisphere summers. The 1997/98 run has mid-latitude minimum from early June to late August, with the minimum ξ sitting around 45°N , while the 1998/99 run has mid-latitude maximum in early June, with the high values of ξ sitting around 60°N . This contrast appears on 600K, 800K, and 1000K (only 800K plotted here). In section 5, we will revisit this difference with the help of artificial tracer runs.

5. GCMs: MACCM2 and SKYHI models

5.1. Model descriptions

In this section, we further our model measurement comparison by including tracer output from two GCMs: the NCAR Middle Atmosphere version of Climate Community Model (MACCM2) [Boville 1995] and Geophysical Fluid Dynamics Laboratory (GFDL) “SKYHI” model [Mahlman and Umscheid 1987]. The N₂O from SKYHI is generated online with GCM, while the N₂O from MACCM2 is a product of offline CTM that is passively advected by the wind field from the GCM [Waugh *et al.* 1997]. The MACCM2 simulation has T42 horizontal resolution (64×64 longitude by latitude points), and there are 44 vertical levels from the surface to $p \approx 0.01$ hPa (80km), of which 28 are at fixed pressure levels above 16 km. The SKYHI model used here has a horizontal resolution of $1^\circ \times 1.2^\circ$ latitude by longitude (N90), and 40 levels in the vertical direction. It also used a hybrid vertical coordinate, which is terrain following near the ground, merging into pure isobaric coordinates above 321 mb. The lowest full model is at roughly 80 m above the ground, the vertical spacing gradually increases with height and is roughly 2 km through most of the stratosphere [Hamilton *et al.* 1995].

Plates 5a and b show ξ from N₂O on the 800K surface from MACCM2 and SKYHI, respectively. They are also overlaid with corresponding zonal-mean zonal winds. Because of the high resolution of SKYHI data (300 × 180 longitude by latitude), the ξ for SKYHI has a higher value, we choose to represent it in a different color scheme to highlight its ξ structure (see NM for discussion of effect of data resolution on ξ). The

discontinuity in the ξ distribution in the early June is due to the fact that the SKYHI simulation starts from early June and ends at early June. We have plotted the data from January 1 to December 31 to facilitate comparison between models.

As with the GSFC runs, the ξ from both GCMs exhibit many common features with ξ from CLAES N₂O calculation. They both have a strong polar barrier enclosed by high ξ . The polar barrier develops in autumn, grows with time and decays in late winter/early spring (northern hemisphere) or early summer (southern hemisphere). Prior to the formation of Antarctic polar barrier, there is a ξ maximum around the same ϕ_e domain in both simulations. In fact, if we follow the track of both the ξ maximum and minimum (red and blue tracks) on Plates 1 and 5, they swing back and forth with time in a very similar fashion along the ϕ_e . This attests to the validity of the core dynamics of these GCM models. They generate the right seasonal cycle not only in the sense of zonal mean wind, but in the mixing properties (e.g. the migration of mixing and barrier zones diagnosed from ξ).

There are, however, differences between ξ from the two GCMs and ξ from CLAES N₂O and they are discussed in the following two subsections.

5.2. MACCM2

Apart from the general agreement with CLAES N₂O calculation, the N₂O calculation from MACCM2 shows that Antarctic polar barrier has dual origins during May, which is only suggested from CLAES N₂O ξ on 800K.

An obvious disagreement between MACCM2 and CLAES calculation is the lack of

a ξ maximum inside the Antarctic polar vortex. Although this maximum is small in area, it is quite obvious in ξ derived from CLAES data. The superimposed zonal mean wind indicate that the MACCM2 Antarctic polar night jet is too strong (the strongest among models and observations presented in this work), and this strong jet might create a wide vortex edge zone covers the entire polar region. We know the vortex edge tends to have small ξ and thus acts as an isentropic transport barrier. Here the enlarged area of low ξ coincident with a strong polar night jet seems to indicate that the area which is usually considered to be vortex edge is enlarged by the strong jet, and therefore produces a wider zone of ξ minimum that leaves almost no room for high values of ξ to develop inside the polar vortex. However, the strong polar night jet can not be the necessary cause for the absence of high ξ inside polar vortices. As discussed in the next subsection, SKYHI N_2O shows high ξ inside both polar vortices though its polar night jets are also strong.

Another area of disagreement with CLAES is the formation/destruction of the vortex: as evident from Plate 2, the MACCM2 simulation does not generate the observed top-down formation and destruction of Antarctic polar vortex.

5.3. SKYHI model

Similar to CLAES N_2O diagnostic, the SKYHI N_2O calculation shows a strong ξ maximum inside Antarctic polar vortex, it also has ξ maximum inside Arctic polar vortex. Comparing to MACCM2 winds, the polar night jets for both hemispheres are smaller for SKYHI simulation, though it is still much stronger than the NCEP and

GSFC assimilated winds. Both the MACCM2 and SKYHI runs have strong polar night jets, but have different ξ structure inside the Antarctic polar vortex. It seems to indicate something else other than the magnitude of wind field is important in determining the effective diffusivity inside polar vortices. It might indicate some inherent difference in the dynamics inside the polar vortices, however, we cannot draw any definitive conclusions at this stage regarding to this feature.

The track of the ξ minimum along the Arctic polar vortex edge in both GCMs is more systematic than the CLAES and the GSFC simulations, suggesting more stable Arctic polar vortices in the two GCMs. This can be verified by the comparison of winds from the GCM winds (Plate 5), and the NCEP (Plate 1) and GEOS DAO assimilated winds (Plate 4).

6. Artificial tracer experiments

By comparing ξ from different models, we have gained helpful insight into the model performance. Because ξ is a diagnosed parameter, while it reflects the dynamics of the background flow, it certainly takes in some other effects, such as chemical sources and sinks. Being long-lived tracers, we expect such influence is small for both N_2O and CH_4 . In the following experiment, following *Haynes and Shuckburgh* [2000a, 2000b] and *Allen and Nakamura* [2001] we advect an artificial tracer with GSFC assimilated wind fields and compare the ξ thus obtained with the one calculated from the simulated N_2O . The artificial tracer experiment has some advantages over the chemical tracers in the calculation of ξ . First we can construct an artificial tracer with a global pole-to-pole

monotonic distribution trend, and thus avoid the trouble of finding equivalent equator and validate the equivalent length diagnostic in the tropics. Second, even a good chemical inert tracer, such as N_2O becomes chemically active in the upper stratosphere and therefore loses its potential as a passive tracer. While an artificial tracer can serve our needs of diagnosing the dynamics without worrying about chemistry throughout the vertical domain of the stratosphere.

The difference between the ξ calculations for the same wind fields will help diagnose the relative sensitivity of the ξ to the background dynamics and specific tracer used to get the ξ , and therefore more insight will be gained on the subject of model comparison.

We use the same finite volume advection scheme that was used by *Allen and Nakamura* [2001]. The tracer is advected on a sphere with a high-resolution finite volume scheme that incorporates the van Leer flux limiter. In our study, we use 20480 triangles to cover the whole sphere, which has a corresponding mean node-to-node separation of 240 km (see *Allen and Nakamura* [2001] for details). The triangular grid eliminates pole problems introduced by models with equally spaced latitude/longitude grids. Comparing to the spectral transform scheme, the van Leer scheme is much more efficient in terms of CPU time.

Plate 6 displays the ξ calculated from an artificial tracer initialized as a sine function of geographic latitude. The tracer is advected with the same GEOS DAS winds that drives the (a) 1997/98 and (b) 1998/99 3D CTM runs. The results for the first month should be disregarded (see [*Allen and Nakamura*, 2001] and [*Haynes and Shuckburgh*, 2000] for discussion on initialization).

The general structure of the two sets of artificial tracer ξ distribution is very similar. Note that the artificial tracer is sampled on a higher resolution than the CTM N_2O , and as we mentioned above, this results in a slightly higher overall ξ . We compensate this difference by using a slightly different color scheme in Plate 6.

However there are some notable differences. The most prominent one is in the northern summer. The ξ from the artificial tracer have obvious minimum in the middle latitudes during northern summer. In 1999, this ξ minimum extends the whole northern hemisphere from the middle of the June till the end of the August, while in 1997, there are two distinct minima in ξ , one centered around $\phi_e = 20^\circ$ and the other in the polar region, with a narrow region of slightly high ξ separating the two minima. For the CTM N_2O calculation, a ξ maximum develops during the 1999 northern hemisphere summer, and occupies the whole northern hemisphere. In the 1997 summer, the ξ has a polar maximum plus a mid-latitude minimum. Therefore the difference between N_2O based ξ and artificial tracer based ξ is larger in the 1999 summer, of which it occurs in the whole northern hemisphere, and smaller in the 1997 summer, of which it occurs poleward of $\phi_e = 70^\circ$.

Another difference between Plate 4 and Plate 6 is inside the Antarctic polar vortex. The N_2O calculation shows high ξ , while the artificial tracer calculation has no such ξ maximum inside the Antarctic polar vortex.

The 1997/98 simulation of N_2O resembles the CLAES N_2O calculation in that it has a ξ maximum inside the Antarctic polar vortex and a ξ maximum poleward of $\phi_e = 70^\circ\text{N}$ plus a ξ minimum equatorward. Both GCM simulations of N_2O in MACCM2

and SKYHI reproduce this pattern of ξ in the northern hemisphere.

Haynes and Shuckburgh [2000a] performed similar experiments with artificial tracers, and their calculations on 450K and above produced an ξ minimum in the northern summer, as found in our artificial tracer run. *Allen and Nakamura* [2001] did similar advection experiments using 7 years of wind and expanded vertical coverage to the 1900K isentropic surfaces. Their 7-year climatology of ξ on 850K and above also produced minimum in the northern summer.

Because results from our artificial tracer simulation are similar to the results produced by *Allen and Nakamura* [2001] and *Haynes and Shuckburgh* [2000a, b], and our CTM N₂O analysis is similar to the CLAES N₂O diagnostic, we infer that the common difference observed between artificial tracer based ξ and N₂O based ξ reflects an inherent difference between the two sets of ξ diagnostics. There are three inherent differences between them. First, one set of experiments is done for artificial tracers, in other words, no chemical sources and sinks. On the other hand, the other set of results is obtained from the analysis of N₂O. As we already stated, though it's a good chemical tracer, some sources and sinks might introduce some chemical effect in the ξ calculation. The second differences between the two sets of experiments is the way the advection is implemented. The artificial tracer experiments are all done on a two dimensional isentropic surface, while all the N₂O calculations (both CLAES observation and model simulations) are advected by three dimensional wind fields. This means the diabatic movement might introduce the differences we saw here. Third, the vertical diffusion introduced by the vertical N₂O gradient might account for some of the difference. The

artificial tracer experiments don't have this in consideration.

Of all the three possible mechanisms, we want to emphasize the diabatic movement, which is simulated in the N₂O experiment but not in the artificial tracer run. We speculate that large diabatic descent inside the Antarctic polar vortex contributes to the large ξ observed both in CLAES and GSFC and SKYHI N₂O. Because N₂O is a fairly good inert tracer around 800K, the most likely source for such difference should come from the different dimensions employed in the two sets of experiments. The southern polar vortex is characterized by strong polar night descent, while it is not uncommon to observe tracer of mesospheric origin in the lower stratosphere. This large diabatic descent for chemical tracers is equivalent to a large isentropic sources or sinks for two dimensional tracer simulations, such as the artificial tracer experiments we described here. This large source and sink term will definitely affect the ξ calculation, though the degree of the influence depends on the vertical tracer gradient.

The northern hemisphere summer does not have a strong diabatic descent, yet it shows difference between N₂O and artificial tracer. Though there is no systematic diabatic descent (or ascent) during summer. There might be diabatic fluctuation caused by some wave activity. Such a speculation is not without ground, as there is observational evidence of wave activity in the summer (e.g. *Wagner and Bowman* [2000], *Hoppel et al* [2001]). More experiments are needed to clarify the mechanism for the differences we observed here.

We also note a possible link between the MACCM2 run and the 2D experiments. Both shows no sign of high ξ inside polar vortices, though observed elsewhere. Because

the 2D experiments do not have a strong polar night jet as the MACCM2 experiment does, it suggests the different simulation of diabatic movement in the MACCM2 and SKYHI might cause the different ξ behavior inside the polar vortices.

7. Summary

In this study, we have performed a model-measurement comparison based on the seasonal distribution of the equivalent length (ξ) diagnostic. This diagnostic provides a way to quantify mixing in the stratosphere from the distribution of long-lived tracers. With the aid of this tool, we have conducted a comparison study between satellite measurements and CTMs driven by assimilated and GCM winds.

We choose N_2O measurements from UARS CLAES as our comparison benchmark, because it has a long chemical lifetime in the lower stratosphere and CLAES measurement is the best global measurement of long-lived tracers available today. A detailed analysis of ξ from CLAES N_2O reveals many mixing and transport properties. An inter-comparison of these results with CH_4 , another long-lived tracer measured by CLAES, adds to our confidence of using it against model output.

In the ξ analysis of CLAES N_2O , the evolution of polar vortex edge and surf zone is captured in details. The annual appearance of polar vortex in high latitudes is illustrated by the strip of ξ minimum on the ξ map. The origin of polar vortex traced by the ξ minimum is from polar region in the lower stratosphere and from subtropics in the middle stratosphere. The different timing in the formation and decay of Antarctic polar vortex along the vertical direction is also illustrated clearly on the ξ calculation

on 5 different isentropic surfaces. High diffusivity found in the summer hemisphere is puzzling, because it is more diffusive than the winter surf zone, which has a strong wave breaking as a stirring agent. This diagnostic is nonetheless supported by both *Haynes and Schuckburgh* [2000a, 2000b] and *Allen and Nakamura* [2001]. It is also reflected partially or entirely in most model outputs of this work. Some alternative mechanism other than the large scale wave breaking for the high diffusivity in the summer stratosphere is proposed.

The GSFC CTM runs driven by assimilated winds provide many details on structures of mixing and barrier zone, many features agrees with the CLAES N₂O results. It also clearly identifies sudden warming events and discriminates weak polar barriers from strong polar barriers. In both GSFC CTM runs, the rate at which the Antarctic polar vortex expands and shrinks is too small comparing to the CLAES diagnostic. This lack of meridional movement of polar vortex edge is likely associated with a too strong Antarctic polar night jet in both experiments. The less systematic Arctic polar barriers in both runs comparing to CLAES N₂O's are due to the sudden warming events, which occurred in 1997/98 and 1998/99. A major difference between the two GSFC CTM runs is the absence of summer high value of ξ in 1997/98 run and presence of it in 1998/99 run. It is not clear at this point whether this is due to the difference in the assimilated wind fields used for the two runs (which comes from the slightly different assimilation systems), or true interannual variability.

The ability of simulating the top-down destruction of Antarctic polar vortex, as seen in the CLAES N₂O, makes the 1998/99 run of GSFC CTM outstanding among the

models. The identification of minimal ξ distribution in the southern hemisphere along 5 different isentropes clearly illustrates the different timing of the decay of Antarctic polar vortex along the vertical direction.

The GCM wind driven CTM runs also capture all the major structures of extratropical mixing and barrier zone. However, the two CTMs differs significantly with each other and with CLAES N_2O inside the Antarctic polar vortex. CLAES N_2O shows signs of moderate high value of ξ inside of Antarctic polar vortex. The MACCM2 runs has no such feature with ξ minimum prevailing throughout the Antarctic polar vortex, while the SKYHI runs has a very strong ξ inside the Antarctic polar vortex. Both runs have strong polar night jet, further investigation is needed to find out the exact cause for this different behavior for the two GCMs.

Experiments with artificial tracer advection on isentropic surfaces provide extra information about the GSFC CTMs when combined with the ξ obtained from three dimension simulation of N_2O . With the same wind field but a perfect conserved artificial tracer, the 2D isentropic advection experiment generates ξ distribution very similar to the one from N_2O . The interesting part comes from the difference between the two. Such differences includes the lack of high ξ inside both Antarctic and Arctic polar vortices, and lack of summer high value of ξ in the northern summer in the 1997/98 run. Three possible mechanisms are proposed for the difference. A special attention is given to the diabatic movement that is absent in the 2D experiment but present in the 3D CTM. Further investigations, including a 3D advection of artificial tracer will help to diagnose the mechanism behind the differences seen here, and might be able to shed

light on the puzzling summer high ξ observed here in most of our diagnostics.

Acknowledgments.

We thank D. R. Allen and Y. Hu for sharing the Van Leer advection code, and N. Nakamura for providing the SKYHI GCM data.

References

- Allen, D. R. and N. Nakamura, A seasonal climatology of effective diffusivity in the stratosphere, *J. Geophys. Res.*, *106*, 7917-7935, 2001.
- Boville, B. A., Middle atmosphere version of the CCM2 (MACCM2): Annual cycle and interannual variability, *J. Geophys. Res.*, *100*, 9017-9039, 1995.
- Butchart, N., and E. E. Remsberg, The area of the stratospheric polar vortex as a diagnostic for tracer transport on an isentropic surface, *J. Atmos. Sci.*, *43*, 1319-1339, 1986.
- Douglass, A. R., R. B. Rood, S. R. Kawa, and D. J. Allen, A three-dimensional simulation of the evolution of the middle latitude winter ozone in the middle stratosphere, *J. Geophys. Res.*, *102*, 19,217-19,232, 1997.
- Douglass, A. R., S. R. Kawa, GSFC 3D Chemistry and Transport Model, in *Models and Measurements Intercomparison II*, NASA/TM-1999-209554, 84-87, 1999
- Farman, J. C., B. G. Gardiner, and J. D. Shanklin, Large losses of total ozone in Antarctica reveal seasonal ClO_x/NO_x, *Nature*, *315*, 207-210, 1985.
- Hamilton, K., R. J. Wilson, J. D. Mahlman, and L. J. Umscheid, Climatology of the SKYHI Troposphere-Stratosphere-Mesosphere General Circulation Model, *J. Atmos. Sci.* *52*, 5-43, 1995.
- Haynes, P., and E. Shuckburgh, Effective diffusivity as a diagnostic of atmospheric transport. Part I: stratosphere, *J. Geophys. Res.*, *105*, 22777-22794, 2000.
- Haynes, P., and E. Shuckburgh, Effective diffusivity as a diagnostic of atmospheric transport. Part II: troposphere and lower stratosphere, *J. Geophys. Res.*, *105*, 22795-22810, 2000.
- Hoppel, K. W., K. P. Bowman, R. M. Bevilacqua, Northern hemisphere summer ozone variability observed by POAM II, *Geophys. Res. Lett.*, *26*, 827-830, 1999.

- Kalnay E., M. Kanamitsu, R. Kistler, W. Collins, D. Deaven, L. Gandin, M. Iredell, S. Saha, G. White, J. Woollen, Y. Zhu, M. Chelliah, W. Ebisuzaki, W. Higgins, J. Janowiak, K. C. Mo, C. Ropelewski, J. Wang, A. Leetmaa, R. Reynolds, R. Jenne, D. Joseph, The NCEP/NCAR 40-year reanalysis project, *Bulletin of the American Meteorological Society*, 77(3), 437-471, 1996.
- Kumer J. B., Kawa S. R., and Roche A. E., Mergenthaler J. L., Smith S. E., Taylor F. W., Connel P. S., Douglass A. R., UARS first global N₂O₅ data sets: application to a stratospheric warming event in January 1992, *J. Geophys. Res.*, 102, 3575-3582, 1997.
- Ma, J., The modified Lagrangian-mean diagnostics of the stratospheric transport and chemistry, Ph.D. thesis, 131 pp., The University of Chicago, August 1999.
- Mahlman, J. D. and L. J. Umscheid, Comprehensive modeling of the middle atmosphere: The influence of horizontal resolution, in *Transport Processes in the Middle Atmosphere*, edited by G. Visconti and R. Garcia, pp. 251-266, D. Reidel, Norwell, Mass., 1987.
- Manney, G. L., R. W. Zurek, and A. O'Neill, Stratospheric warmings during February and March 1993, *Geophys. Res. Lett.*, 21, 813-816, 1994.
- Manney, G. L., W. A. Lahoz, R. Swinbank, A. O'Neill, P. M. Connaw, and R. W. Zurek, Simulation of the December 1998 stratospheric major warming, *Geophys. Res. Lett.*, 26, 2733-2736, 1999.
- McIntyre, M. E. and T. N. Palmer, The "surf zone" in the stratosphere, *J. Atmos. Terr. Phys.*, 46, 825-849, 1984.
- Nakemura, N., Two-dimensional mixing, edge formation, and permeability diagnosed in an area coordinate, *J. Atmos. Sci.*, 53, 1524-1537, 1996.
- Nakamura, N., Leaky containment vessels of air: A Lagrangian-mean approach to the

- stratospheric tracer transport, in *Dynamics of atmospheric flows: Atmospheric transport and diffusion processes*, edited by M. Rahman, pp. 193-239, Computational Mechanics Publications, UK, 1998.
- Nakamura, N., and J. Ma, Modified Lagrangian-mean diagnostics of the stratospheric polar vortices 2. Nitrous oxide and seasonal barrier migration in the cryogenic limb array etalon spectrometer and SKYHI general circulation model, *J. Geophys. Res.*, *102*, 25,721-25,735, 1997.
- Pierrehumbert, R. T., Lattice models of advection-diffusion, *Chaos*, *10*, 61-74, 2000.
- Plumb, R. A., On the seasonal cycle of stratospheric planetary waves, *Pure and applied geophysics, PAGEOPH*, *130*, 233-242, 1989.
- Plumb, R. A., A "tropical pipe" model of stratospheric transport, *J. Geophys. Res.*, *101*, 3957-3972, 1996.
- Randel, W. J., Global atmospheric circulation statistics, 1000-1 mb, *NCAR technical note*, NCAR/TN-366 + STR, 1992.
- Randel, W. J., and P. A. Newman, The stratosphere in the southern hemisphere, *Cooperative Research Centre for Southern Hemisphere Meteorology Technical Report*, *2*, 1997.
- Roche, A. E., J. B. Kumer, J. L. Mergenthaler, G. A. Ely, W. G. Uplinger, J. F. Potter, T. C. James, and L. W. Sterritt, The Cryogenic Limb Array Etalon Spectrometer (CLAES) on UARS: Experiment description and performance, *J. Geophys. Res.*, *98*, 10,763-10,775, 1993.
- Roche, A. E., J. B. Kummer, R. W. Nightingale, J. L. Mergenthaler, G. A. Ely, P. L. Bailey, S. T. Massie, J. C. Gille, D. P. Edwards, M. R. Gunson, M. C. Abrams, G. C. Toon, C. R. Webster, W. A. Traub, K. W. Jucks, D. G. Johnson, D. G. Murcay, F. H.

- Murcray, A. Gold Man, and E. C. Zipf, Validation of CH₄ and N₂O measurements by the cryogenic limb array etalon spectrometer instrument on the Upper Atmosphere Research Satellite, *J. Geophys. Res.*, *101*, 9679-9710, 1996.
- Shuckburgh, E., W. Norton, A. Iwi, and P. Haynes, The influence of the quasi-biennial oscillation on isentropic transport and mixing in the tropics and subtropics, *J. Geophys. Res.*, , submitted.
- Wagner, R. E., and K. P. Bowman, Wavebreaking and mixing in the northern hemisphere summer stratosphere, *J. Geophys. Res.*, *105*, 24799-24807, 2000.
- Waugh, D. W., and R. A. Plumb, Contour advection with surgery: A technique for investigating fine scale structure in tracer transport, *J. Atmos. Sci.*, *51*, 530-540, 1994.
- Waugh, D. W., T. M. Hall, W. J. Randel, P. J. Rasch, B. A. Boville, K. A. Boering, S. C. Wofsy, B. C. Daube, J. W. Elkins, D. W. Fahey, G. S. Dutton, C. M. Volk, and P. F. Vohralik, Three-dimensional simulations of long-lived tracers using winds from MACCM2, *J. Geophys. Res.*, *102*, 21,493-21,513, 1997.
- Waugh, D. W., and W. J. Randel, Climatology of Arctic and Antarctic polar vortices using elliptical diagnostics, *J. Atmos. Sci.*, *56*, 1594-1613, 1999.
- Waugh, D. W., W. J. Randel, S. Pawson, P. A. Newman, and E. R. Nash, Persistence of the lower stratospheric polar vortices, *Jgr* *104*, 27,191-27,201, 1999.
- Zurek, R. W., G. L. Manney, A. J. Miller, M. E. Gelman, and R. M. Nagatani, Interannual variability of the northern polar vortex in the lower stratosphere during the UARS mission, *Geophys. Res. Lett.*, *23*, 289-292, 1996.

J. Ma and D. W. Waugh, Department of Earth and Planetary Science, Johns Hopkins

University, Baltimore, MD 21218. (email: junma@rua.eps.jhu.edu; waugh@jhu.edu)

A. R. Douglass and S. R. Kawa, Code 916, NASA GSFC, Greenbelt, MD 20771.

Received _____

Plate 1. Time series of equivalent length obtained on (a) 1000K, (b) 800K, and (c) 600K isentropes for CLAES N_2O . Zonal mean of NCEP/NCAR reanalysis wind is superimposed on the plot in gray.

Plate 2. Equivalent length distributions on five isentropic surfaces, 500K, 600K, 700K, 800K, 900K, and 1000K, for N_2O of CLAES (thick purple line), MACCM2 (thin red line), GSFC 3D CTM 97/98 run (thin blue line), and 98/99 run (thin green line) in June (left column) and November (right column). Both CLAES and GSFC entries are averaged over 10 days, the MACCM2 entry is averaged over 15 days. The date shown on top of each column represents the median date of sampled period for each dataset.

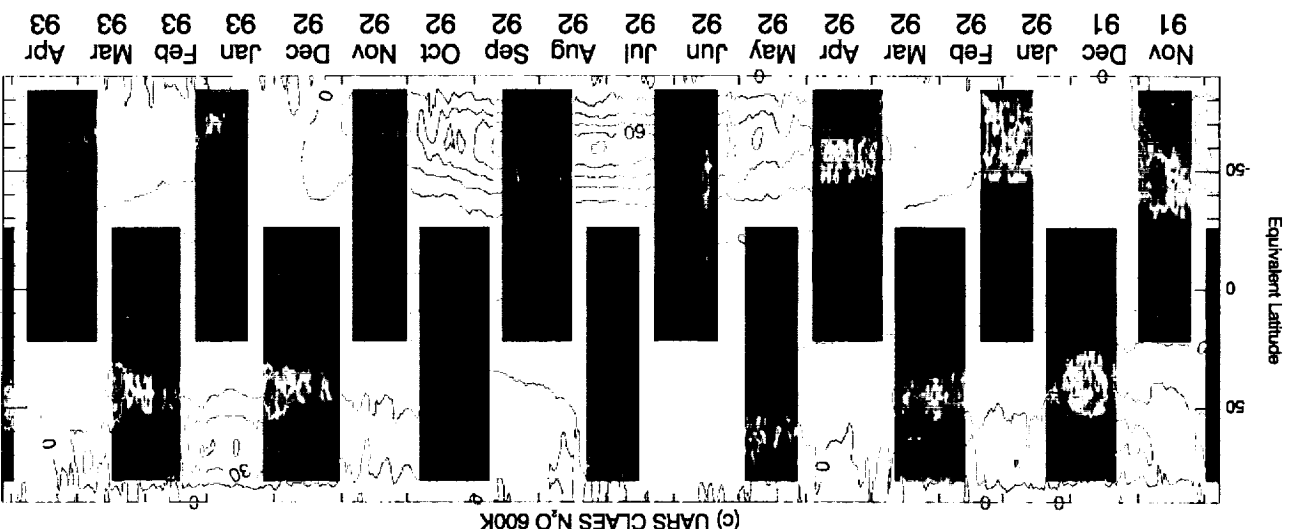
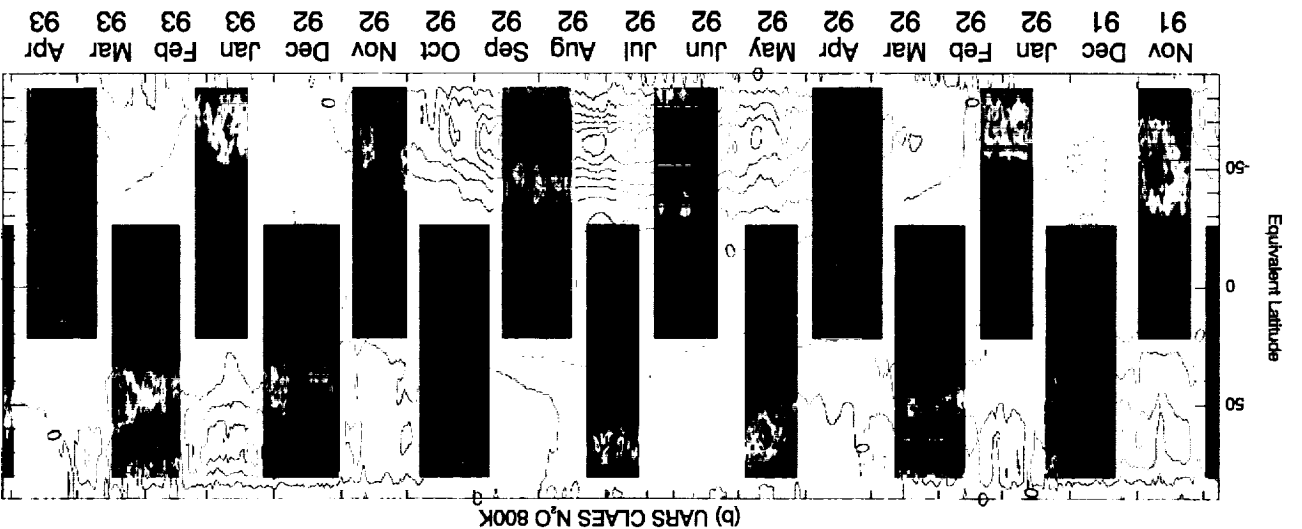
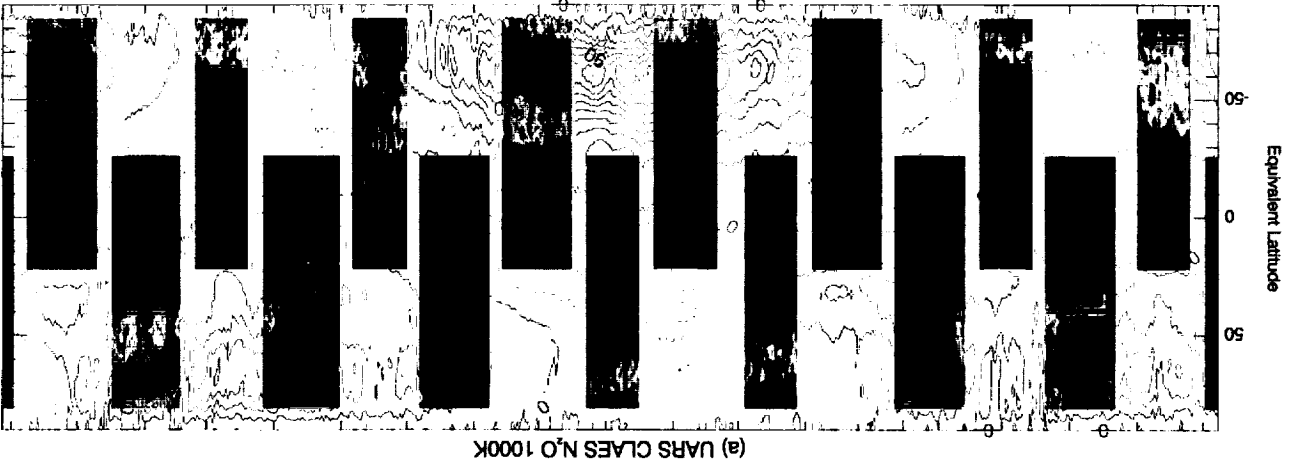
Plate 3. Potential temperature and equivalent latitude cross section of CLAES N_2O and CH_4 . (a) rmN_2O during January 25-27, 1992, (b) N_2O during January 25-27, 1993, (c) CH_4 during January 25-27, 1992, (d) CH_4 during January 25-27, 1993.

Plate 4. Time series of equivalent length obtained on 800K isentropes for N_2O from (a) 97/98 and (b) 98/99 run of GSFC CTM. Zonal mean of the corresponding assimilated wind is superimposed on the plot in white.

Plate 5. Time series of equivalent length obtained on 800K for N_2O from (a) MACCM2 CTM and (b) GFDL SKYHI CTM. Corresponding zonal mean wind is superimposed on each map in white. Note that the color scheme for SKYHI calculation is different from the other two experiments.

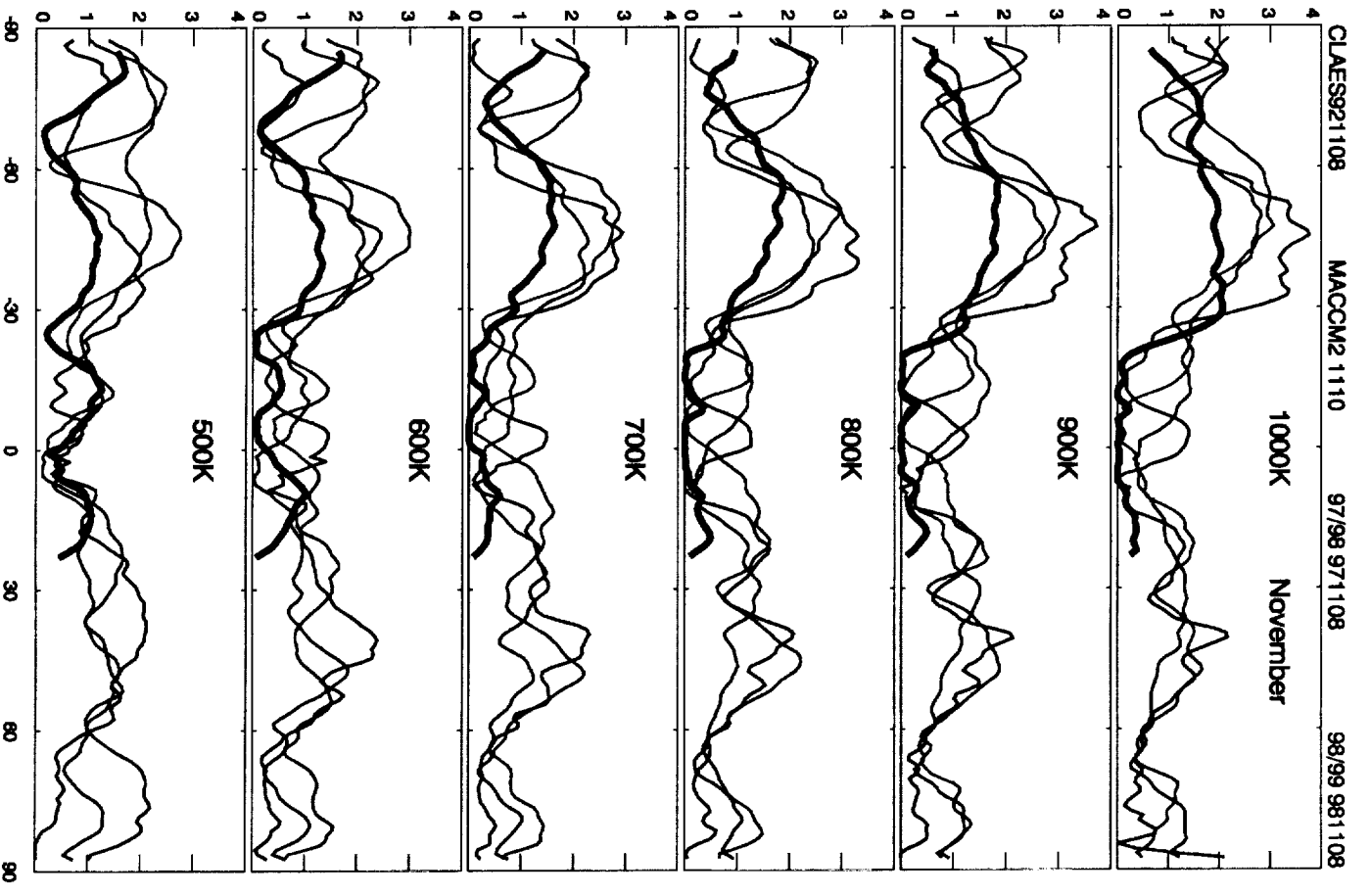
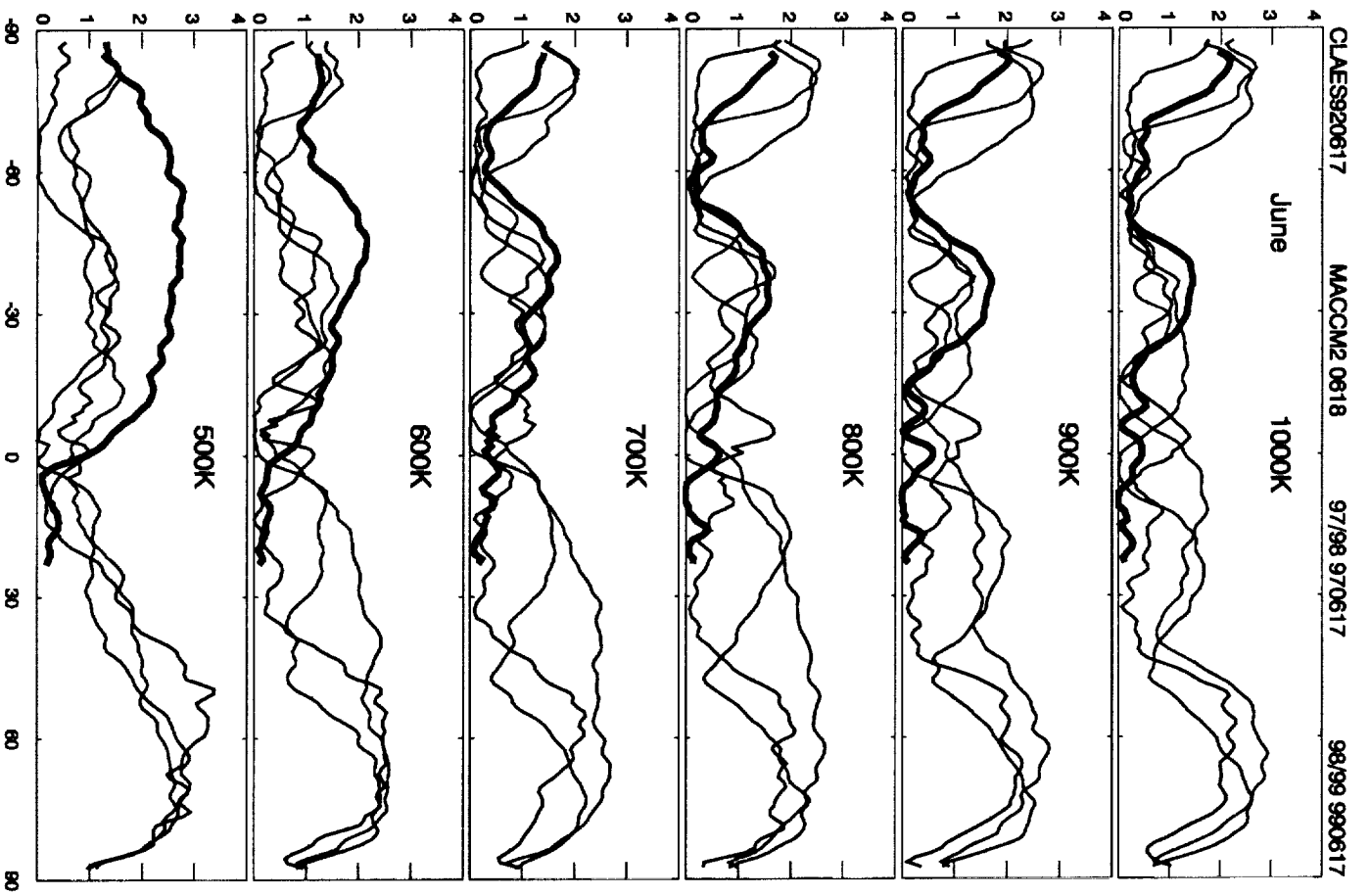
Figure 1. Mean deviation of equivalent length difference between CLAES N₂O and CH₄ (it is obtained by first subtracting CH₄ based equivalent length from N₂O based equivalent length and then taking mean value out of it).

Plate 6. Time series of equivalent length obtained on 800K isentropes for artificial tracer (of the function of $\sin \phi$, ϕ is the geographic latitude) advected by the GEOS DAS wind field of (a) 97/98 run and (b) 98/99 run. Zonal mean of the assimilated wind is superimposed on the plot in white.

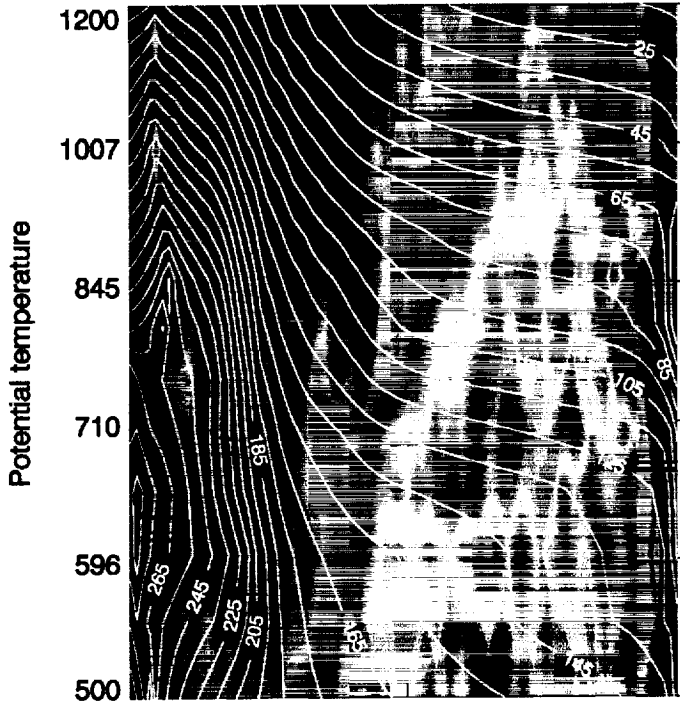


Normalized Equivalent Length (5)

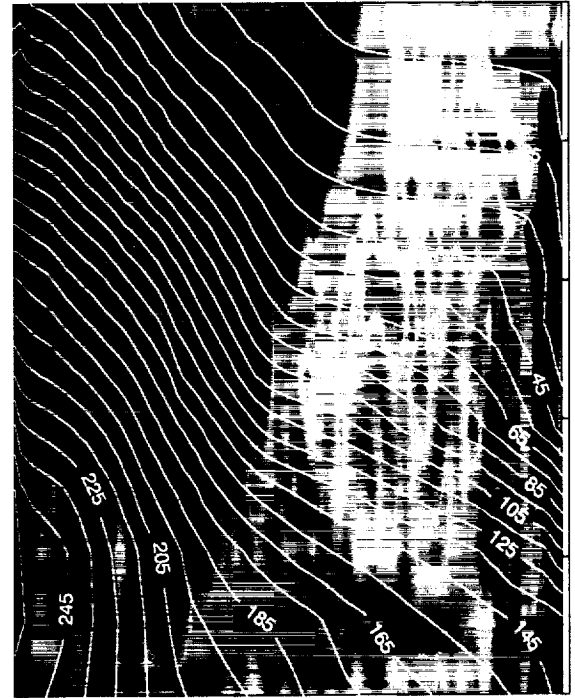




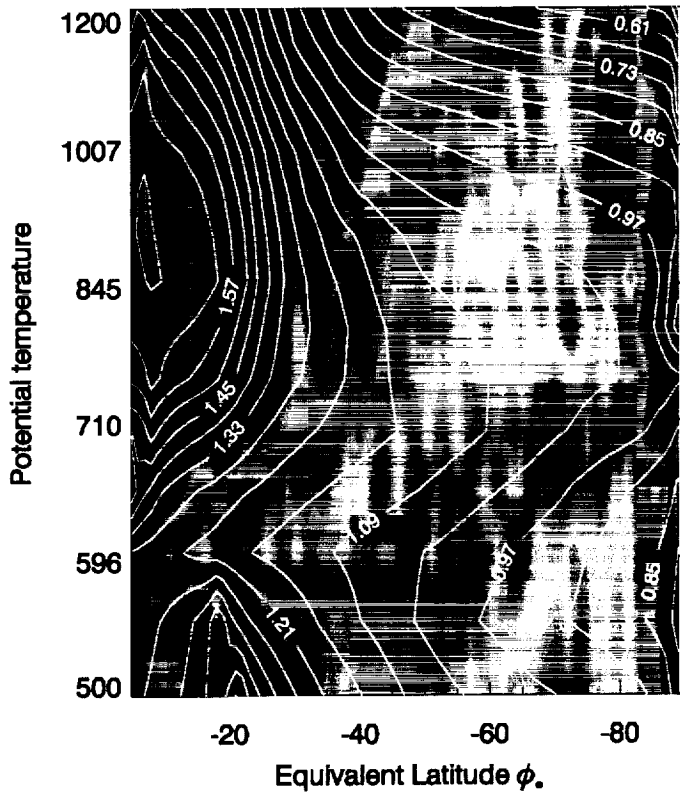
CLAES N₂O January 25-27, 1992



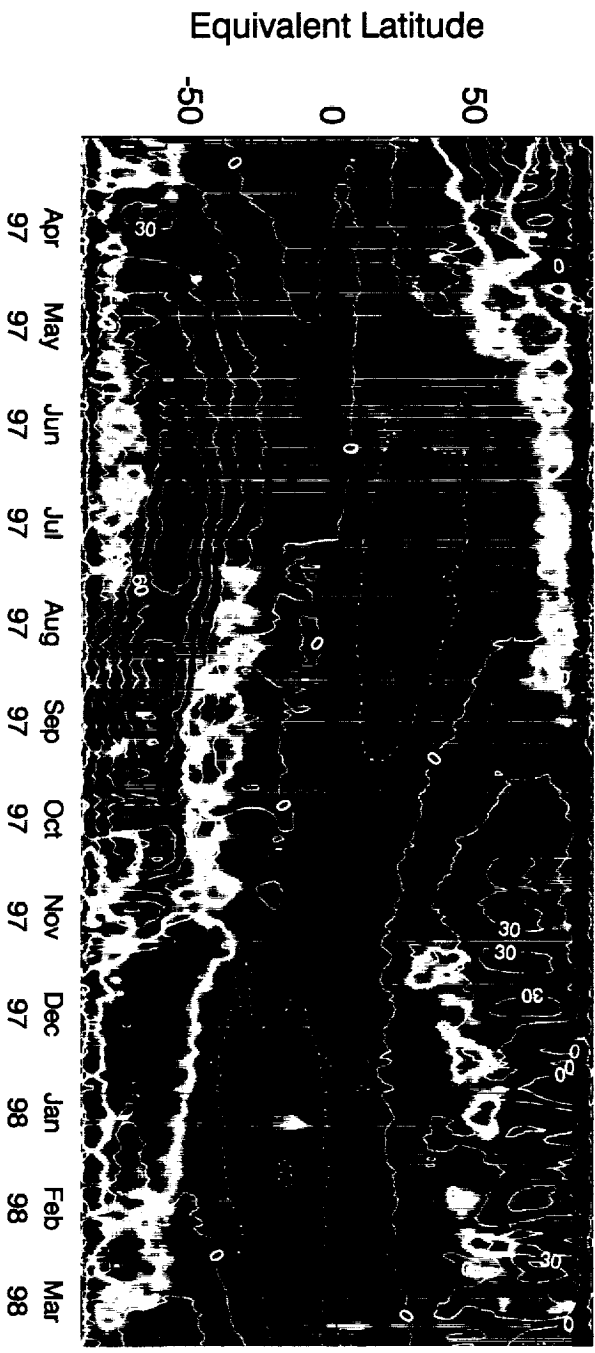
CLAES N₂O January 25-27, 1993



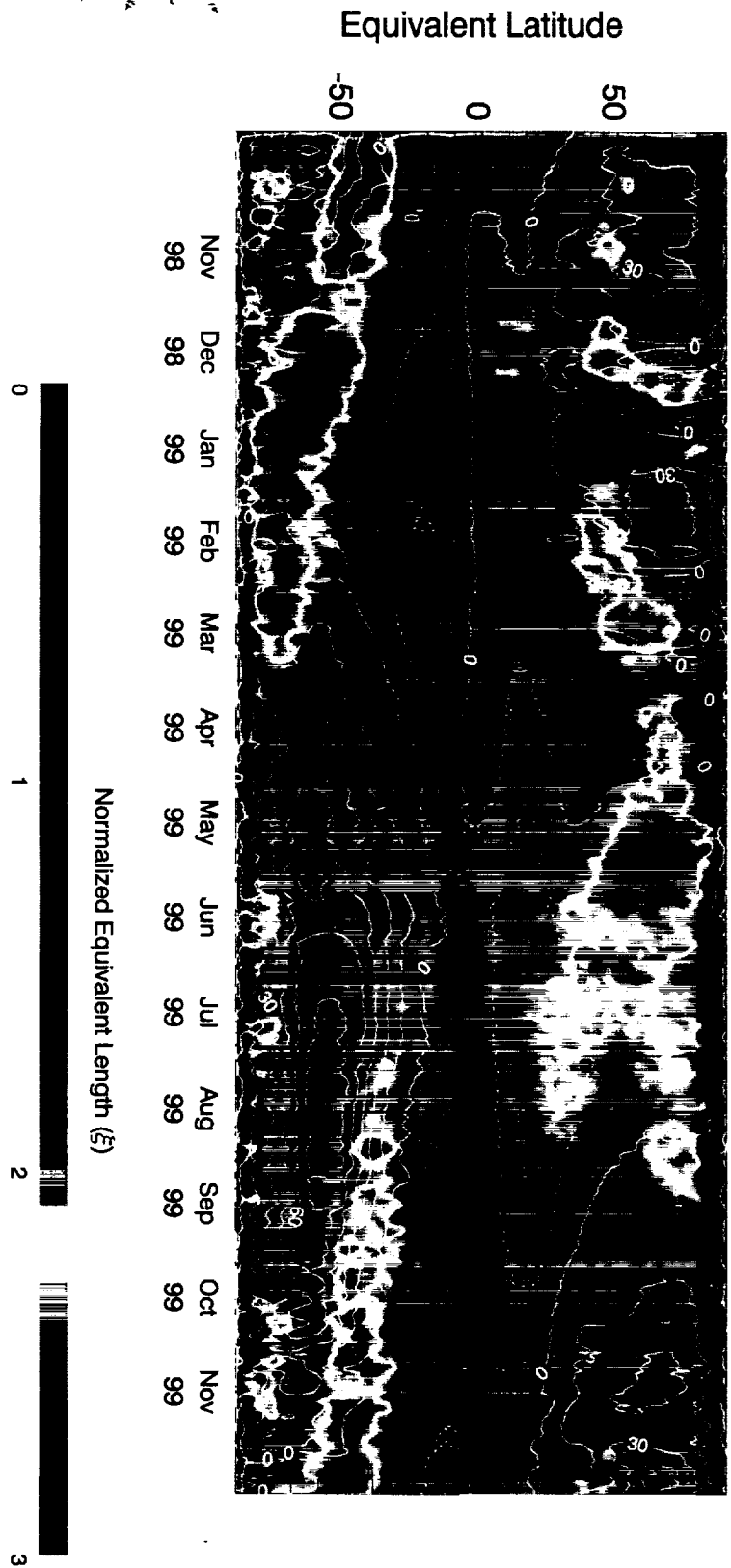
CLAES CH, January 25-27, 1992



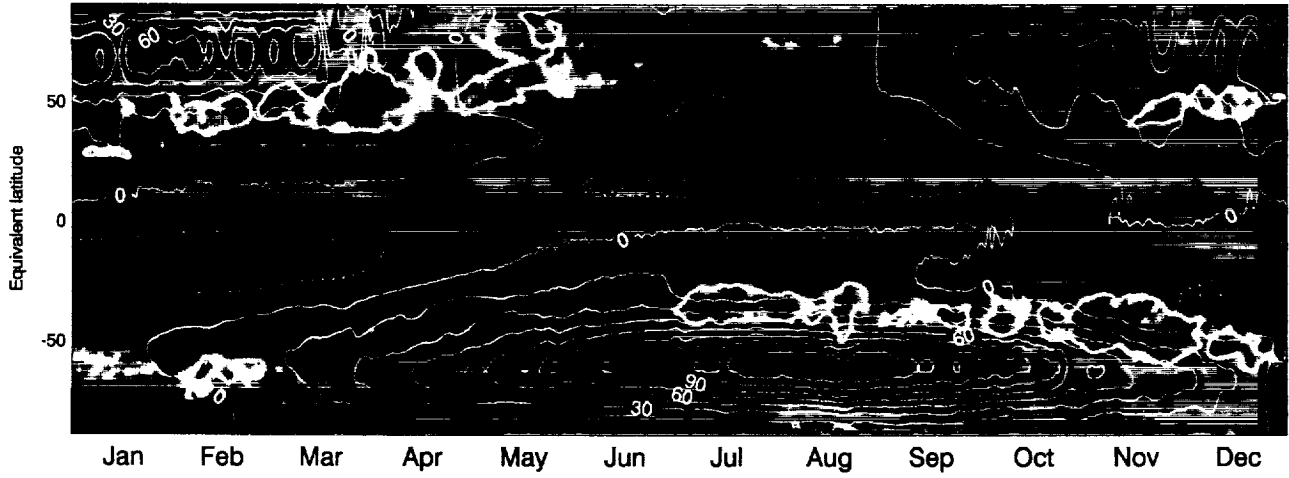
(a) GSFC 3D CTM 97/98 N₂O 800K



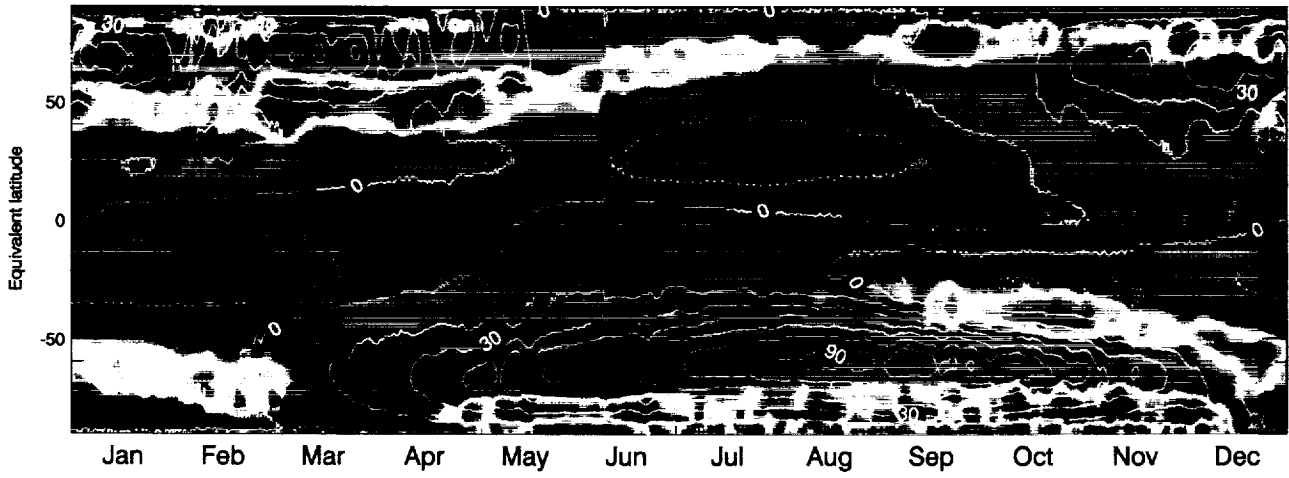
(b) GSFC 3D CTM 98/99 N₂O 800K



(a) MACCM2 N₂O 800K



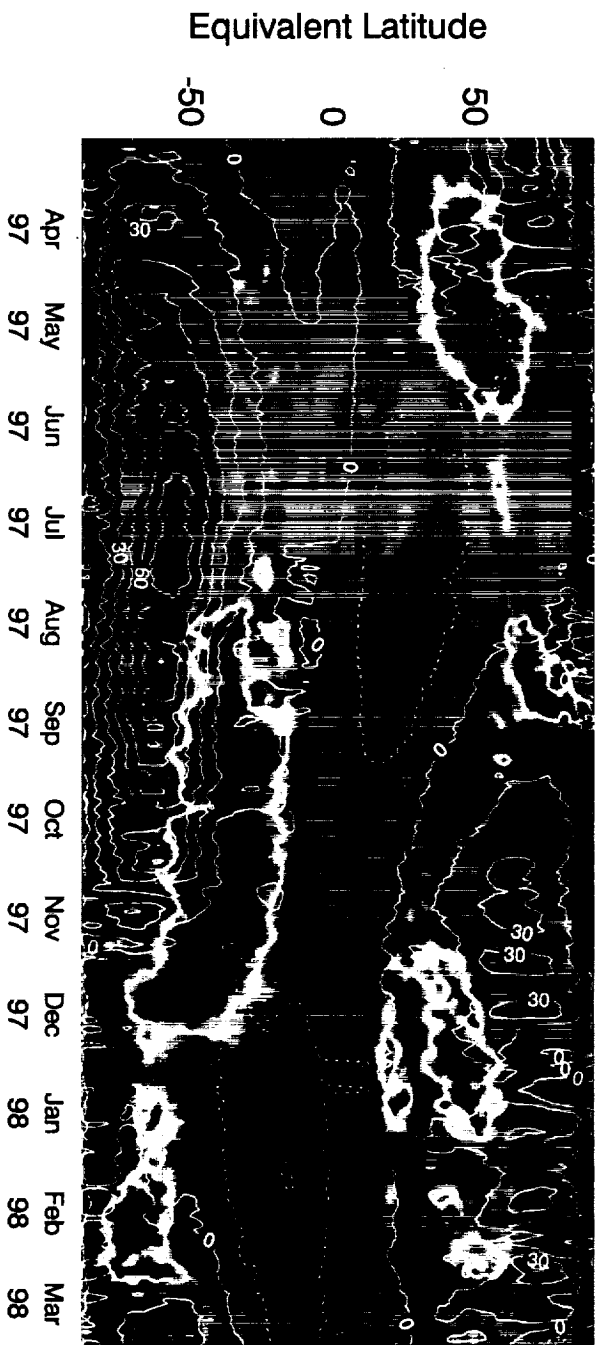
(b) SKYHI N₂O 800K



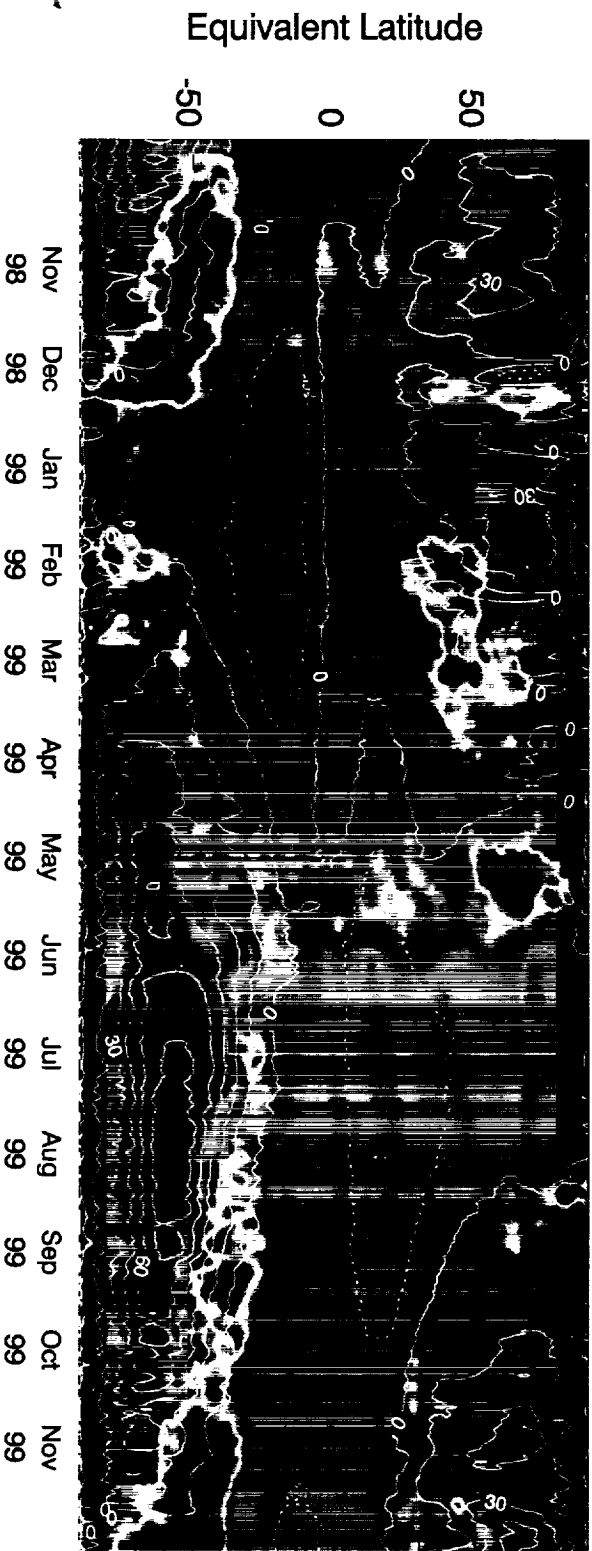
Normalized Equivalent Length (ξ)



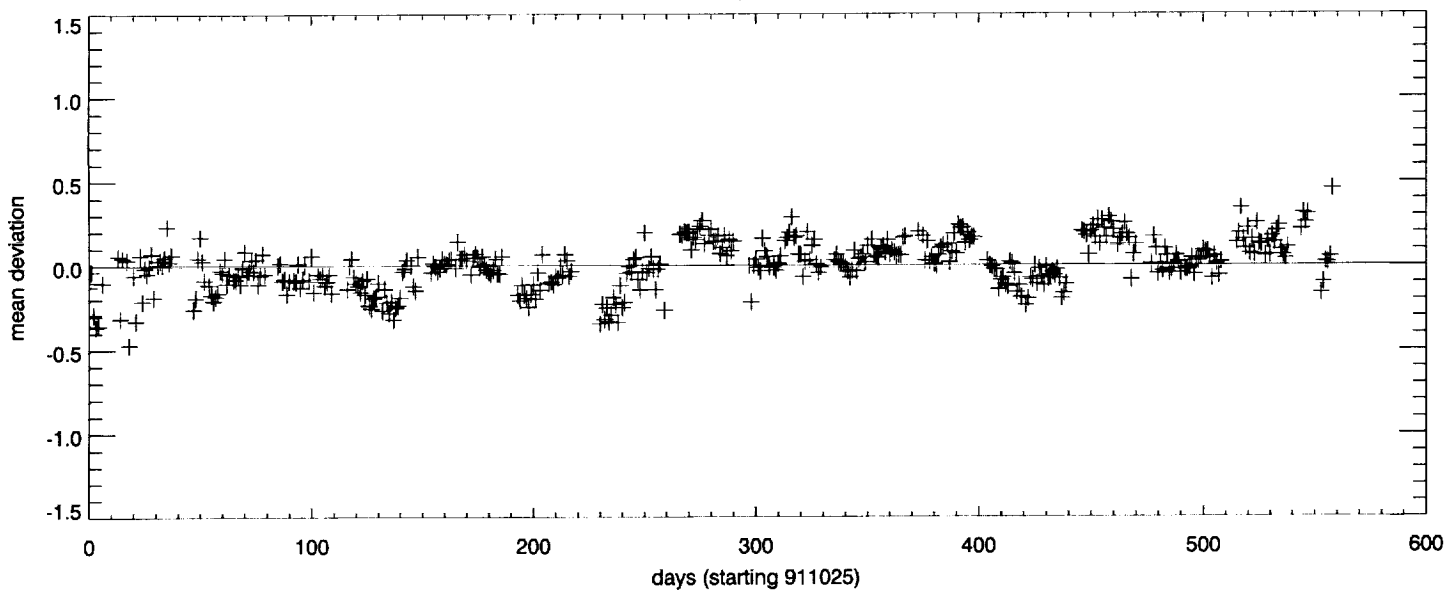
(a) GSFC 97/98 SIN(ϕ) 800K



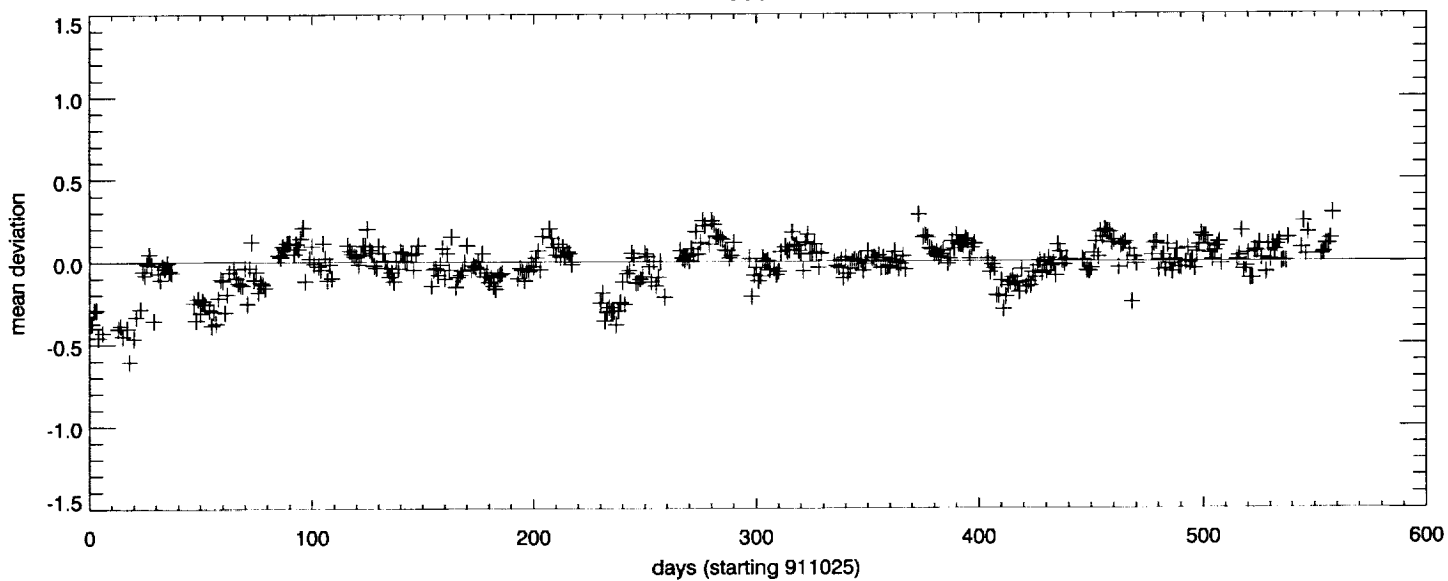
(b) GSFC 98/99 SIN(ϕ) 800K



1000K



800K



600K

